Plasmonic Band Structure Controls Single-Molecule Fluorescence

Lutz Langguth,[†,*] Deep Punj,[‡] Jérôme Wenger,[‡] and A. Femius Koenderink[†]

[†]Center for Nanophotonics, FOM Institute for Atomic and Molecular Physics (AMOLF), Science Park 104, 1098 XG Amsterdam, The Netherlands and
[‡]CNRS, Aix-Marseille Université, Ecole Centrale Marseille, Institut Fresnel, Campus de St Jérôme, 13397 Marseille, France

ABSTRACT Plasmonics and photonic crystals are two complementary approaches to tailor single-emitter fluorescence, using strong local field enhancements near metals on one hand and spatially extended photonic band structure effects on the other hand. Here, we explore the emergence of spontaneous emission control by finite-sized hexagonal arrays of nanoapertures milled in gold film. We demonstrate that already small lattices enable highly directional and enhanced emission from single fluorescent molecules in the central aperture. Even for clusters just four unit cells across, the directionality is set by the plasmonic crystal band structure, as confirmed by full-wave numerical simulations. This realization of plasmonic phase array antennas driven by single quantum emitters opens a flexible toolbox to engineer fluorescence and its detection.

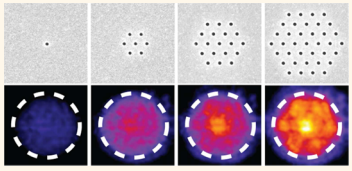

KEYWORDS: nanoantenna · plasmonics · plasmonic crystal · nanoaperture · fluorescence enhancement · Bloch mode

Achieving a complete manipulation of the generally weak optical signal from a single quantum emitter is a key objective in nanophotonics. To this end, two major routes have been investigated: plasmonic metal nanostructures[1−11] and dielectric photonic crystals.[12−21] Both routes have demonstrated breakthrough results in tailoring the photoluminescence intensity, spectrum, or directionality of single emitters. The plasmonic approach has put the most emphasis on the nanoscale antenna element to control single-emitter radiation[1,2,22−24] *via* the strong electromagnetic enhancement in the near field of metals. In contrast, the photonic crystal approach centers on the use of coherent scattering to boost the interaction strength of intrinsically weakly scattering building blocks. State-of-the-art structures use thin high-index membranes perforated by nanoapertures, in which the guided modes fold into a complex band structure. Spontaneous emission control then revolves around the targeted coupling of an emitter to select Bloch modes, with well-controlled out-coupling characteristics. Very recently, interest has emerged in the interplay between these two approaches, implying the use of a coherent array of plasmonic resonators to shape the luminescence emission properties. Two key examples are provided on one hand by the use of diffractive modes in 2D arrays of plasmon particles to shape emission of thin emissive layers[10,11,25−27] and on the other hand by the demonstration of Yagi−Uda antennas with a single quantum dot emitter in the optical regime,[3] where coherent near -field coupling between scattering nanoparticles is determinant to achieve directional emission.[6]

Here, we investigate the emergence of coherent antenna array effects to shape the fluorescence emission of single molecules in finite-sized bidimensional arrays of apertures milled into a metal film that supports surface plasmon guided modes. Transmission properties of quasi-infinite aperture arrays and single holes have been thoroughly investigated in the framework of extraordinary optical transmission.[28] As reviewed by Garcia-Vidal *et al.* and de Abajo,[29,30] transmission measurements show sharp, dispersive features that are frequently likened to a folding of the free surface plasmon dispersion relation into a band structure, where the scattering potential that sets the interaction strength is set by the single-aperture polarizability. The influence of the array size was studied by Przybilla[31] and by Henzie.[32] The transmission of just a small patch of nanoaperture lattice is the well-known very broad single-hole resonance, on which even for very small patches the sharp features of extraordinary optical transmission are superimposed. As a function of

* Address correspondence to L.Langguth@amolf.nl.

Received for review June 28, 2013 and accepted September 10, 2013.

Published online September 10, 2013
10.1021/nn4033008

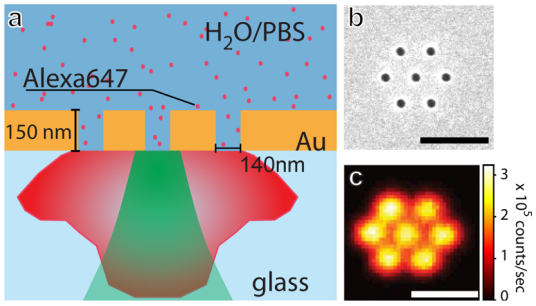

Figure 1. (a) Sketch of the sample consisting of a 150 nm thick gold film on glass with apertures of 140 nm diameter at 440 nm pitch. A drop of 1 μM solution of Alexa Fluor 647 in a water saline solution is placed on top of the sample. (b) SEM image and (c) confocal fluorescence scan of a hexagonal array consisting of a central hole with one shell of apertures around it. The scale bars correspond to 1 μm.

patch size, these features sharpen and show small shifts. On the basis of this work we examine if, even in small nanoaperture patches, periodic lattice physics controls phased array antenna design for single molecules. We show the possibility of effective beam shaping by as few as 25 scatterers. In a direct plasmonic analogy of photonic crystals milled in dielectrics, we consider hexagonal arrays of nanoapertures milled in gold film, immersed in a dilute solution of fluorescent molecules (Figure 1). Only the central aperture is illuminated by a tightly focused pump laser beam. The driving source for the fluorescence emission stands in the molecules located in the central aperture, which serves as a feed element for the rest of the antenna array. In this paper, we show that the plasmonic crystal band structure of surface plasmon polaritons (SPP) is effective even in very small clusters of apertures to tailor the radiation pattern of single molecules and provide a substantial absolute increase in measured brightness per molecule. To support our experiment, we start from a general model to calculate the radiation pattern for arbitrary arrangements of nanoapertures driven by a single molecule, which enables the design of radiation patterns without symmetry constraints. For the specific case of periodic arrangements as in our experiment, the calculation ultimately reduces to a folding of the dispersion relation of the SPP dispersion into bands that emerges in the radiation patterns. While, formally, a band structure, *i.e.*, a sharp $\omega(k)$ relation, exists only in infinite, lossless systems, in the plasmonic case, the band structure pertains to lossy modes (radiative loss and absorptive loss). For perforated films, this band structure is well known, reveals itself in experiments as broadened bands, and is close to the folded free surface plasmon dispersion relation, in which narrow stop gaps open up.[33−35] In agreement with our data and full-wave simulations, the model predicts strong directionality for frequencies near the closing of the second plasmon band, at the center of the Brillouin zone. We find that the local density of photonic states (LDOS) enhancement that we measure is independent of the lattice and primarily determined by the central aperture. Fluorescence directionality and absolute extracted flux per molecule as caused by the phased array behavior can thus be tuned independently from LDOS enhancement.

The significance of this study is twofold. First, from a conceptual point of view, it investigates the buildup of directionality by coherent scattering in antenna arrays driven by a single emitter. Second, from an application-driven point of view, we demonstrate enhanced directional emission of fluorescence into a narrow angular cone that can be efficiently collected by a simple low numerical aperture optical lens. On the basis of fluorescence correlation spectroscopy data, we provide quantitatively calibrated evidence of a large per-molecule brightness increase of 40 times in the forward direction. This property is desirable to achieve high-sensitivity fluorescence detection with simple optical systems. The performance of our structures is on par with earlier work[7,8,36] that used nanoapertures surrounded by milled corrugations in a so-called "bull's eye" configuration. Conceptually, however, nanoaperture arrays have as a major advantage that the emission characteristics rigorously factorize in a single hole "structure factor" and an "array factor" that encodes the geometric hole arrangement. This separation tremendously simplifies modeling and opens up a rich set of beam-shaping design options for metasurface substrates, much like the beam shape and polarization control possible with broad-area photonic crystal emitters.[21] Furthermore, we note that the aperture arrays reported here are technically much simpler to fabricate, for instance lending themselves to large-scale replication *via* soft conformal imprint techniques or template stripping.[37−39]

RESULTS AND DISCUSSION

To obtain directed fluorescence emission normal to the sample plane, we design the plasmonic band structure so that the center wavelength for fluorescence emission for our fluorophore (around 660 nm) falls near a plasmonic band edge that closes at the Γ-point ($\mathbf{k}_{||} = 0$). This condition sets the pitch between neighboring apertures to about one SPP wavelength. Specifically, we fabricated optically thick gold films (150 nm thick) on a glass substrate and drilled nanoapertures of 140 nm diameter in lattices of 440 nm pitch using focused ion beam milling. A series of samples was generated with increasing number of rings of holes around a central aperture from 0 (single aperture) to 3, placing the holes in a hexagonal lattice.

To record the influence of the plasmonic band structure on single-molecule fluorescence emission, we cover each sample with a water solution containing Alexa Fluor 647 dye at 1 μM concentration (Figure 1a), which infiltrates the nanoapertures. Diffusion ensures a

continuous exchange of fluorophores in the aperture with the reservoir in the droplet and thus avoids photobleaching of the aperture fluorescence. The dipole orientation of the fluorophores in the liquid is random and constantly changing. Thus all measured quantities are averages over the dipole orientation. The sample is placed on a sample-scanning confocal inverted microscope and excited using a laser beam at 633 nm wavelength. As the confocal scan in Figure 1c shows, the different apertures constituting the array are well resolved by our confocal setup. We obtain very bright fluorescence with count rates above 300 kHz when exciting the center aperture and counts below 1 kHz when illuminating the gold film. Importantly, for each experiment reported below, we keep the position of the sample fixed and centered on the laser focus, making sure to excite only the central hole of each array. As part of our measurement protocol, prior to assessing directionality, we benchmark the number of fluorescing molecules in the center aperture on the basis of "fluorescence correlation spectroscopy".[40] This is performed by computing the second-order temporal correlation of the fluorescence intensity, as previously established.[7] We find that for all structures, independently of the total number of holes in the cluster, we detect almost the same number of contributing molecules ($\langle N \rangle = 3.5 \pm 0.7$).

To analyze the angular fluorescence emission, we record the fluorescence intensity distribution in the back focal plane (Fourier plane) of a 1.2 NA water immersion objective on a charge-coupled device (CCD) camera. The radial coordinate in these images scales as the numerical aperture sin θ for the emission, and thus the CCD images represent the intensity $I(\theta,\varphi)$ emitted from the plasmonic crystal structure for different angular directions, where θ is measured from the sample normal and φ is the azimuthal angle. Figure 2 summarizes our main experimental results, namely, the evolution of the radiation pattern as captured in the back focal plane images as a function of lattice size. A single aperture (Figure 2a,e) does not show any significant directional feature, although emission is more directional than a Lambertian emitter would be. In Fourier imaging with a high NA aplanatic objective, a truly Lambertian emitter would in fact show as a disk with highest intensity at the edge of the back focal plane image.[41,42] In stark contrast to the rather featureless single-hole radiation pattern, when the central aperture is surrounded by three shells of holes, the radiation pattern appears clearly structured (Figure 2d,h). In particular, a significant beaming is observed in the forward direction, and the central beam is accompanied by a set of six side lobes reproducing the 6-fold symmetry of the lattice. Remarkably, we obtain directional emission despite the averaging over all emitter orientations. On one hand this demonstrates robustness of the observed directionality, while on the other hand further improvements might be possible if strategies to localize sources on the nanoscale would be employed.[3] Although only the center aperture is excited, the entire lattice structure contributes to determine the angular distribution of the fluorescence emission. We relate this strong directionality in the normal direction to constructive interferences between the fluorescence light directly emitted from the central aperture into the far field and the surface-wave coupled fluorescence emission that is scattered into the far field by the neighboring apertures. A necessary condition for such constructive interference is that the aperture-to-aperture pitch corresponds to approximately one SPP wavelength on the gold/glass interface. This condition can be understood equivalently in k-space as requiring operation exactly at the condition of second-order Bragg diffraction for the surface plasmon wave, *i.e.*, at the closing of a plasmonic band near the Γ-point of the lattice. Importantly, the observation of strong directionality demonstrates that the neighboring apertures *coherently* re-emit the surface-wave fluorescence light stemming from a single molecule. Incoherent superposition of the fluorescence light emitted by different molecules would result only in the same featureless and broad radiation pattern observed for a single (isolated) aperture.

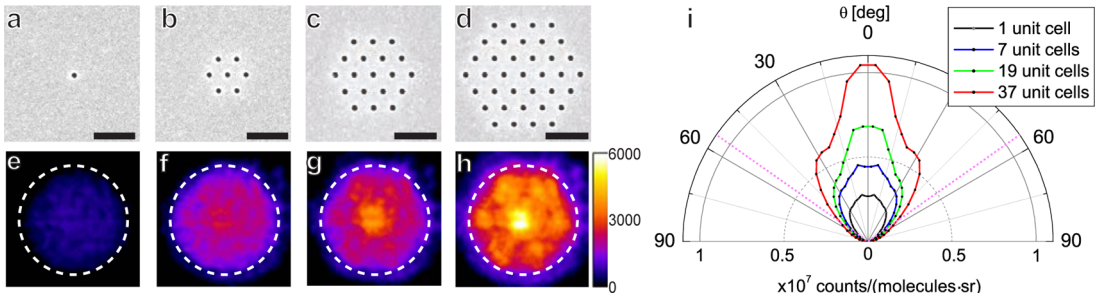

Figure 2. (a) Scanning electron micrographs of a single-hole structure and hexagonal clusters with (b) 7, (c) 19, and (d) 37 unit cells (one, two, and three shells) around the central aperture (the scale bar is 1 μm). (e−h) Back focal plane (Fourier plane) images representing the radiation patterns for the structures in (a)−(d). Note that only the central aperture was illuminated by the laser beam in these experiments. The color bar represents a linear scale from 0 to 6000 counts per pixel. (i) Radiated intensity in counts per second per molecule per solid angle for hexagonal lattices of increasing number of apertures.

To quantify the directionality relative to the sample normal, we average back focal plane images over the azimuthal coordinate, taking into account the weighting caused by the objectives aplanatic lens construction.[42] Polar plots of the azimuthally averaged radiation patterns in Figure 2i demonstrate increased directionality correlated with growing structure size, in excellent agreement with the behavior expected for a coherent phased array antenna. On the basis of the calibration of the average number of detected molecules for each sample, we can directly relate the radiation patterns to detected photon flux *per molecule* and per solid angle.[7,8] This quantifies the fluorescence enhancement along each emission direction. Furthermore, we can also compute the directivity figure of merit for each antenna. In classical antenna theory, the directivity corresponds to the ratio of the radiated power density along the direction of strongest emission relative to the power density radiated by an ideal isotropic source emitting the same amount of total power.[43] For a single aperture, we measure a fluorescence enhancement of 10× integrated over the whole numerical aperture (as compared to the reference in solution without aperture) and a corresponding directivity of 3.4 dB.[8] For a hexagonal lattice with three shells, we record a fluorescence enhancement up to 40× in the forward direction and a directivity of 4.3 dB. The enhancement and directivity clearly increase with lattice size, as expected from a spatially distributed phased array effect.

That a hexagonal lattice provides strong directionality is expected since the radial distance from the central aperture to the next row of apertures is uniquely defined, so that contributions from all apertures sum up constructively. In other words, the hexagonal lattice benefits from an almost circular Brillouin zone. This should be contrasted to the case of square lattices, which we also investigated to further confirm the defining role of the band structure for the radiation pattern. We performed measurements on square lattices of different sizes, all with the same pitch of a = 440 nm as the hexagonal structures and with the same hole size of 140 nm. Figure 3 shows scanning electron micrographs of the fabricated square structures (total size 1, 5, 21, 37 unit cells). As in the case of hexagonal arrays, we measured radiation patterns and observed increasing overall collected flux per molecule as the structure size increases. However, the radiation pattern is best characterized as a ring with a minimum in the forward direction. The maximum enhancement of 2.8× for the square lattice is located at an angle of $\theta \approx 20°$, whereas the enhancement in the forward direction is only 1.9×. This stark contrast with the hexagonal lattice data can be interpreted in k-space, first, as the Brillouin zone being more circular for the hexagonal case and, second, through the fact that at the same pitch the square lattice reciprocal lattice vectors differ by a factor of $(3/4)^{1/2}$ in length.

We now return to the strongly directional radiation patterns evident for hexagonal lattices and compare our measurements to 3D electromagnetic simulations performed with the finite-element method using a commercial solver (see Methods section). Figure 4a presents the results for a single aperture surrounded by two shells of apertures in a hexagonal lattice (corresponding to the experiment depicted in Figure 2c,g). The simulated radiation patterns bear a substantial dependence on the emission wavelength (we show in Figure 4b a fluorescence spectrum of Alexa Fluor 647 for reference). The radiation patterns show a marked transition from highly directional beaming in the forward direction for wavelengths of 700 nm and above, to a redistribution of the radiated power into six side lobes and no emission in the forward direction at wavelengths of 685 nm and below. The experimental back focal plane images actually result from spectral averaging over the range from 670 to 710 nm (gray-shaded region in Figure 4). This spectral averaging underlies our experimental observation of strong beaming normal to the sample *accompanied by* six side lobes for the hexagonal lattice.

To confirm experimentally the predicted spectral dependence of the radiation patterns, we record the fluorescence spectrum after placing a diaphragm in the back focal plane to transmit only the radiation of the inner lobe (corresponding to the green circle in Figure 4a). We report spectra for the structure analyzed in Figure 2(d,h). The spectra with a diaphragm (green solid line), without a diaphragm (magenta dashed line),

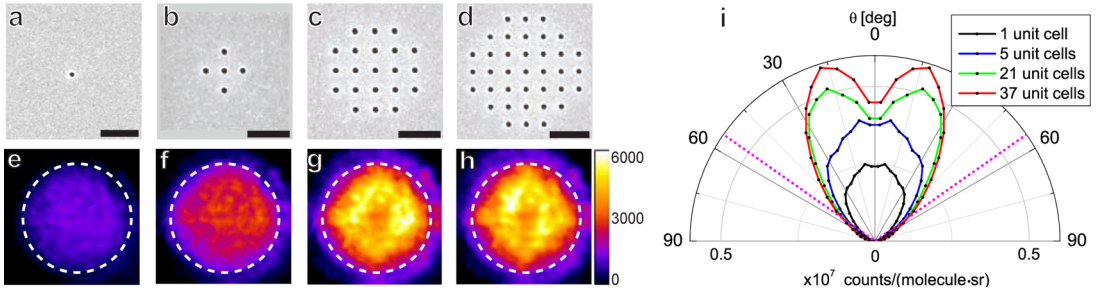

Figure 3. (a–e) Scanning electron micrographs of square lattices of different size (scale bar: 1 μm), (e–h) corresponding radiation patterns, and (i) radiated intensity per molecule per steradian.

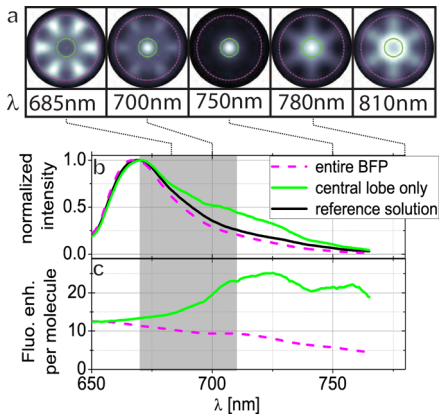

Figure 4. (a) Computed radiation patterns into the glass substrate for selected wavelengths assuming an isotropic ensemble of emitting dipoles in the central aperture surrounded by two shells of apertures in the hexagonal lattice. (b) Normalized fluorescence spectra after placing a diaphragm (corresponding to the green circle in panel a) in the back focal plane to transmit only the radiation of the inner lobe. The reference solution spectrum appears in black, the hexagonal cluster with two shells and open diaphragm (full angular integration) is shown by the magenta dashed line, and the closed diaphragm case is displayed by the solid green line. (c) Enhancement of the fluorescence intensity per molecule with an open (magenta dashed line) or closed diaphragm (solid green line).

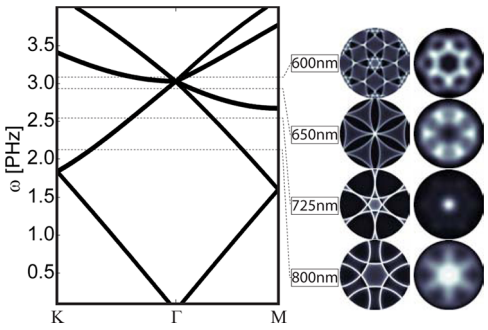

Figure 5. Left column: Band diagram of the folded dispersion relation of a hexagonal 2D lattice with zero interaction. Middle column: Characteristic isofrequency cuts through folded wavevector space at selected frequencies indicated by dashed lines, which are well below, just below, and just above the second-order SPP Bragg diffraction condition. Right column: Characteristic radiation patterns from COMSOL corresponding to the characteristic cuts of the dispersion relation.

and of the reference solution (black solid line) show marked differences in the region 700−740 nm. In particular, when we use the diaphragm to select only the central lobe, the spectrum clearly shows an extra emission shoulder in the red, consistent with the prediction from simulations that beaming is strong only for wavelengths to the red of a sharp cutoff at 700 nm (Figure 4b). The differences are better clarified by computing the fluorescence enhancement as compared to the confocal reference case (Figure 4c). When only the central lobe is selected, we observe a significant spectral enhancement for wavelengths above 700 nm, indicating that the central lobe indeed contains significantly red-shifted fluorescence emission. This experimental finding stands in excellent agreement with the predictions from the simulated radiation patterns.

On the basis of measurements and simulations, we conclude that the hexagonal clusters of apertures realize a nanoscale phased array antenna, where the required coupling between scatterers must be mediated *via* surface plasmon polaritons. To underpin this claim with a simple analytical model, we use a classical result from radiowave antenna theory.[42,43] In the far field of a phased array antenna of identical elements, the electric field along an observation direction $\hat{k}$ (vector of unit length) can be written as

$$E = \frac{e^{ikR}}{R} S(\hat{k}) \sum_{n=1}^{N} A_n e^{-ik \cdot r_n} \qquad (1)$$

where R is the radius of the observation sphere, and $\mathbf{k} = \omega/c\hat{k}$. Here, the first term is an overall spherical wave, and the second term, $S(\hat{k})$, is the form factor of each single element, which is in the case of a single nanoaperture almost but not perfectly isotropic,[36] and corresponds to the measured radiation pattern in Figure 2e. The final term is the structure factor that is determined by the positions r_n and complex amplitudes A_n of the scatterers. If we set the apertures to be driven through the surface plasmon (SPP) waves launched at the central aperture, we can assume a complex amplitude $A_n = (Ae^{ik_{SPP}r_n})/(r_n)^{1/2}$. Importantly, the finite structure phased array response is intimately related to the infinite-lattice band structure. If we lump the finite lattice truncation and the $1/\sqrt{r}$ decay together in a windowing function W_N, we can rewrite eq 1 as

$$E = \left[\frac{e^{ikR}}{R} S(\hat{k})\right] [W_N \sum_{\text{lattice}} e^{i(k_{SPP}r_n - ik \cdot r_n)}] \qquad (2)$$

As recognized by Rigneault,[44] the infinite sum over the entire lattice k is formally equivalent to Harrison's construction[45] for the repeated zone scheme dispersion of the surface plasmon dispersion relation. For an infinite, lossless lattice, the infinite sum results in a discrete set of circles of radius k_{SPP} centered at the reciprocal lattice vectors. The rigorous band structure beyond the folded free surface plasmon dispersion approximation was defined and calculated by Lalanne *et al.*[35] For the finite, lossy lattices studied here, the truncation windowing translates into a blurring of the infinite lattice band structure, formalized as a convolution with the Fourier transform $\mathscr{W}_N$ of the truncation W_N.

Figure 5 shows the folded dispersion relation as a ω, k-diagram, where we calculate k_{SPP} from the surface plasmon dispersion on the Au/glass interface. As per the design choice of lattice pitch, we expect the dispersion relation to cross the Γ-point in the dye emission spectrum, at 650 nm within the free SPP

approximation. In a system with finite interaction strength one expects a red shift of the entire dispersion relation[35] and the opening of a small stop gap at the edge of the Brillouin zone, which pushes the lower band edge further to the red.[11,29,33,46] For frequencies below the band edge, the allowed modes lie on a ring of wave vector close to $k_{||} = 0$. As the wavelength sweeps from 750 nm to ~700 nm, we hence expect increasing directionality as the ring closes. As the band edge is crossed, emission is funneled into the next higher order band that does not close at the Γ-point. Consequently, a steep transition in the radiation pattern is expected to occur from a single lobe to a six-lobed radiation pattern, as is indeed predicted by the full-wave simulations. We refer to the Supporting Information for a complete theoretical analysis for the square lattice case (data reported in Figure 3). In brief, for square lattices the Γ-point crossing of the square lattice is red-shifted out of the dye emission spectrum. Instead the fluorescence is coincident with the next higher band, hence exiting the sample off-normal. Full-wave simulations further confirm the observed radiation patterns and reveal that square lattices allow directional emission normal to the sample further to the IR, commensurate with the red-shifted band edge.

Finally, for completeness, we also have measured the local density of states enhancement that the nanoaperture arrays provide. From the field of photonic crystals it is well known that redirection effects are not necessarily related to strong LDOS modifications. For instance, already at moderate index contrast marked redirection of emission, diffraction, and band-edge slow down of light[47−50] can occur, although variations in spontaneous emission rates in such systems are small.[51,52] For both the hexagonal and square samples and for all patch sizes, we have measured fluorescence decay traces using time-correlated single photon counting, pumping with a 636 nm pulsed diode laser. Independent of array type or size, we record fluorescence lifetimes in the range $\tau = 0.49 \pm 0.01$ ns (Figure 6). Comparison with the lifetime of the open solution of $\tau_{open} = 1.03$ ns yields a significant shortening of the lifetime in the nanoaperture by a factor of 2.1. Through the known internal quantum efficiency, the measured *total* decay rate can be separated as the sum of an intrinsic nonradiative decay rate that is not modified by photonic environment and the intrinsic radiative rate on which the photonic environment acts,[22] where by definition the change exactly equals the LDOS normalized to the vacuum LDOS. Here the LDOS is rigorously defined as the imaginary part of Green's function $\mathcal{I}(G(\mathbf{r_0},\mathbf{r_0}))$ and contains the sum of all decay channels provided by the photonic environment,[41] including those related to decay into any plasmonic modes with strong near-field enhancement, decay directly into the radiative continuum, and any

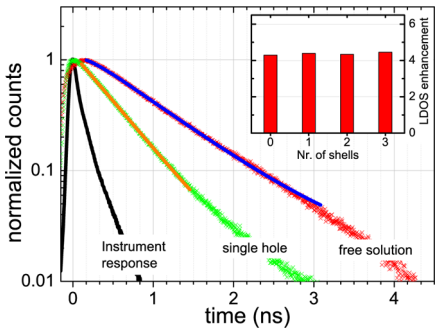

Figure 6. Normalized fluorescence decay traces for the reference solution (red markers) and the single aperture (green markers). The normalized decay traces for the hexagonal lattices with increasing number of apertures are found to be identical to the single-aperture case. Solid lines are fitted decay curves; the black line represents the instrument response function. The inset shows the LDOS enhancement *versus* structure size.

quenching that is induced by the vicinity of the metal. Since the quantum efficiency of Alexa Fluor 647 is $\eta = 33\%$, we conclude that in all experiments the molecules experience a significant LDOS enhancement by a factor $1/\eta((\tau_{open}/\tau) - 1 + \eta) = 4.4$. Importantly, we find that the measured LDOS inside the central aperture is virtually independent of the lattice structure and not altered by the formation of a SPP band structure. Since Wenger *et al.*[53] already reported a complete study of the radiative and nonradiative decay channels in single nanoapertures, we do not pursue a decomposition into the distinct contributions that add up to the measured LDOS change here. The important conclusion for this work is that the nanophotonic control factorizes into two effects. On one hand directionality control and an increase in absolute count rate per molecule are provided *via* coherent reradiation by the entire phased array. As in the case of moderate index photonic crystals, this redirection effect is strong, although the periodicity has no strong effect on LDOS. Indeed, the LDOS is governed entirely by the geometry of the hole to which the fluorophore is directly coupled. A similar factorization to facilitate nanophotonic design was noted for plasmonic Yagi−Uda antennas, where the entire array determines the overall directivity, while Purcell enhancement can be independently engineered by modifying only the feed element.[6]

CONCLUSIONS

Hexagonal clusters of nanoapertures in a plasmonic film realize a nanoscale phased array antenna to control single-molecule emission. The formation of a plasmonic band structure is a simple and powerful tool to tailor the radiation patterns of localized single emitters, enabling up to 40 times brightness enhancement per molecule in the forward direction in our experiment. We demonstrate that even small lattices with less than 25 elements show such highly

directional emission that is set by the plasmonic crystal band structure, in excellent correspondence with numerical simulations. Interestingly, the single-emitter radiation pattern can be tuned independently from the LDOS, as the 4.4-fold Purcell enhancement factor depends only on the geometry of the central hole that acts as a feed element for the entire antenna.

Strong directionality of emission was reported earlier in two distinct plasmonic scenarios: on one hand for Yagi–Uda antennas that are interpreted as a traveling wave phased array antenna and on the other hand for emission of ensembles of fluorophores tuned to diffraction resonances in infinite periodic arrays.[10,11,25–27] Here, we show that the very same mechanisms that are explored for infinite arrays of scatterers are already at play in small phased array antennas, as the band structure is evident in the emission pattern of single emitters in very small clusters of scatterers that are just a few unit cells across. This demonstration that infinite-system dispersion relations of diffractive modes can be used to tailor the behavior of phased array antennas that are very limited in size is complementary to the finding for Yagi–Uda antennas that directionality results from the infinite 1D chain dispersion relation.[3,6] While Yagi–Uda antennas are limited to on-axis beaming, diffractive arrays allow much larger flexibility for beam steering, beam shaping, and polarization control. Thereby our work opens a rich toolbox to engineer single photon emitters to emit selectively in particular angles, in polarization states, or in more exotic beam profiles such as doughnut modes or orbital angular momentum beams. As compared to surface groove milling,[7,8,36] the fabrication of an array of apertures appears as a much simpler and robust technical solution. Indeed, while the structures presented in this article were prototyped with focused ion beam milling, they can be manufactured on a large scale using replication techniques such as imprint lithography.[37–39]

METHODS

Nanofabrication. Our samples consist of a metal film deposited on a glass cover slide (Menzel Gläser #1.5, thickness: 0.17 ± 0.01 mm) by thermal evaporation. We first evaporated 2 nm chromium and then 150 nm gold (10^{-6} mbar, 0.6 Å/s). Several arrays of nanoapertures (140 nm) were milled into the metal film by focused ion beam milling. In particular, the arrays are small periodic hexagonal lattices (1, 7, 19, 37 unit cells; Figure 2a–d) of 440 nm pitch.

Experimental Setup. The experimental setup is based on a confocal inverted microscope with a NA = 1.2 water-immersion objective. The sample is mounted on a computer-controlled XYZ piezo stage (Polytech PI P-517.3CD), and the dye solution (≈1 μM Alexa647 in standard phosphate-buffered saline solution) is dropped on the sample and infiltrates the nanoapertures. A He–Ne laser (λ_{HeNe} = 633 nm, continuous wave (CW)) is focused with a water immersion objective (Zeiss C-apochromat 40×, NA = 1.2) on the sample through the glass slide. For lifetime measurements, the excitation source is a picosecond laser diode operating at 636 nm (PicoQuant LDH-P-635, repetition rate 80 MHz). A single-mode optical fiber (Thorlabs P3-630A- FC-5) ensures a perfect spatial overlap between the pulsed laser diode and the CW He–Ne laser. The fluorescence signal is collected through the same objective and is separated from the pump laser light at a dichroic mirror. For confocal imaging and fluorescence correlation spectroscopy (FCS) we employ a 30 μm pinhole (effectively 375 nm in the sample plane). Single-photon detection is performed by avalanche photodiodes (APD) (Micro Photon Devices MPD-5CTC) in a Hanbury-Brown Twiss configuration featuring a bandpass filter (Omega Filters 640AELP) in front of each APD to further remove all scattered laser light. The fluorescence intensity temporal fluctuations are analyzed with an ALV6000 hardware correlator, which computes the second-order correlation function. We determine the average number of molecules contributing to the signal by fitting the analytical expression[53] for free diffusion FCS.

For radiation pattern imaging a mirror just after the dichroic mirror directs the fluorescence emission through a bandpass filter (690 ± 20 nm) on a camera (Kodak KAF-1603, CCD with microlenses). The optical path between objective and CCD contains only bandpass filtering (690 ± 20 nm), but no lenses, and is about 1 m in length. In the backfocal plane (BFP) the intensity distribution corresponds to the angular emission pattern or "Fourier image" of the structure in the focal plane.[54] We reconstruct a polar plot of radiated flux per solid angle by averaging the radiated power over the azimuthal angle φ and compensating for the 1/cos θ response associated with back-aperture imaging of aplanatic lens systems.[41,42]

For fluorescence lifetime measurements, the APD output is coupled to a fast time-correlated single photon counting module (PicoQuant PicoHarp 300) and correlated against the electronic trigger output of the pulsed laser diode. The temporal resolution of our setup for fluorescence lifetime measurements is 120 ps fwhm. Finally, for measuring the antenna's influence on the fluorescence spectrum, fluorescence was sent to a spectrograph (Horiba iHR320) equipped with a Peltier-cooled CCD detector. To measure the spectrum of the inner lobe of the fluorescence emission, a diaphragm (2.9 mm) was inserted into the beam path right after the dichroic and aligned with the CCD. The diameter of the collimated beam of the entire BFP is ~9 mm. The raw spectrum is normalized by the number of molecules given by correlation analysis, which allows to directly compare the fluorescence enhancement as a function of emission wavelength. The Supporting Information contains a full setup diagram and a description of the measurement protocol.

Numerical Simulations. Full-wave calculations of radiation pattern were obtained using the COMSOL 4.3 finite element solver. As refractive indices we assume $n = 1.33$ and $n = 1.52$ for water and glass and a modified Drude model $\varepsilon = \varepsilon_b - (\omega_p{}^2/(\omega^2 + i\omega\gamma))$ for gold,[55] with $\varepsilon_b = 9.54$, $\omega_p = 2\pi \times 2.148 \times 10^{15}$ Hz, and $\gamma = 0.0092\omega_p$. As simulation domain we use a cylinder with an axis normal to the sample substrate that is a stack of water and the perforated gold film, on top of which we place a hemispherical dome of glass (representative real space geometry shown in the Supporting Information). The simulation domain is closed on all sides with perfectly matched layers (~$\lambda/2$ thickness) and has a radius of 2 μm (approximately 4 wavelengths). As source we place a current-carrying dipole in the center of the central hole mimicking the fluorescent molecule. For dipoles located on the central axis, we can employ symmetry to reduce the computation load, having to solve only in the $x > 0$, $y > 0$ quadrant and employing perfect electric/magnetic boundary conditions on the symmetry planes as appropriate. We retrieve the far field by performing a Stratton–Chu near- to far-field transformation[56] of the fields that we calculate on the glass side on a spherical cap concentric with the central hole, which has a radius of 1.33 μm (3 wavelengths as measured in glass) and is truncated 300 nm above the sample surface. It should be noted that in the

presence of a substrate the Stratton−-Chu near- to far-field transformation is not rigorous, and the results are hence a finite-truncation radius approximation to the angular spectrum representation integral that rigorously describes radiation patterns near surfaces. On the basis of benchmark comparisons of this approach to theory for dipole sources above unpatterned interfaces,[57,58] we estimate accuracy to within 10−20%. We obtain ensemble averaging over random dipole orientation rigorously by summing the calculated angle-resolved far-field fluxes over three orthogonal dipole orientations for which we do the simulations. In practice we found that the *z*-oriented dipole hardly contributes to far-field radiation in both the hexagonal and square lattice, pointing to a large difference in radiative LDOS.

Conflict of Interest: The authors declare no competing financial interest.

Acknowledgment. We are grateful to Martin Frimmer, Clara Osorio, Nicolas Bonod, and Hervé Rigneault for stimulating discussions. We acknowledge a Van Gogh grant of the Frans-Nederlandse Academie (FNA) and the Réseau Franco-Néerlandais (RFN) for facilitating exchange visits. This work is part of the research program of the Foundation for Fundamental Research on Matter (FOM), which is financially supported by the The Netherlands Organization for Scientific Research (NWO). This work is supported by NanoNextNL, a micro- and nanotechnology consortium of the Government of The Netherlands and 130 partners. A.F.K. gratefully acknowledges an NWO-Vidi grant for financial support. The research leading to these results has received funding from the European Commission's Seventh Framework Programme (FP7-ICT-2011-7) under grant agreements 288263 (NanoVista) and ERC StG 278242 (ExtendFRET).

Supporting Information Available: Measurement protocol, calibration FCS measurements, simulated radiation patterns and folded dispersion relation on square arrays, and further details on the COMSOL simulation procedure. This material is available free of charge *via* the Internet at http://pubs.acs.org.

REFERENCES AND NOTES

1. Agio, M., Alú, A., Eds. *Optical Antennas*; Cambridge University Press, 2013.
2. Kinkhabwala, A.; Yu, Z.; Fan, S.; Avlasevich, Y.; Müllen, K.; Moerner, W. E. Large Single-Molecule Fluorescence Enhancements Produced by a Bowtie Nanoantenna. *Nat. Photonics* **2009**, *5*, 654–657.
3. Curto, A. G.; Volpe, G.; Taminiau, T. H.; Kreuzer, M. P.; Quidant, R.; van Hulst, N. F. Unidirectional Emission of a Quantum Dot Coupled to a Nanoantenna. *Science* **2010**, *329*, 930–933.
4. Kosako, T.; Kadoya, Y.; Hofmann, H. F. Directional Control of Light by a Nano-optical Yagi-Uda Antenna. *Nat. Photonics* **2010**, *4*, 312–315.
5. Taminiau, T. H.; Stefani, F. D.; Segerink, F. B.; van Hulst, N. F. Optical Antennas Direct Single-Molecule Emission. *Nat. Photonics* **2008**, *2*, 234–237.
6. Koenderink, A. F. Plasmon Nanoparticle Array Waveguides for Single Photon and Single Plasmon Sources. *Nano Lett.* **2009**, *9*, 4228–4233.
7. Aouani, H.; Mahboub, O.; Bonod, N.; Devaux, E.; Popov, E.; Rigneault, H.; Ebbesen, T. W.; Wenger, J. Bright Unidirectional Fluorescence Emission of Molecules in a Nanoaperture with Plasmonic Corrugations. *Nano Lett.* **2011**, *77*, 637–644.
8. Aouani, H.; Mahboub, O.; Devaux, E.; Rigneault, H.; Ebbesen, T. W.; Wenger, J. Plasmonic Antennas for Directional Sorting of Fluorescence Emission. *Nano Lett.* **2011**, *77*, 2400–2406.
9. Belacel, C.; Habert, B.; Bigourdan, R.; Marquier, R.; Hugonin, J.-R.; Michaelis de Vasconcellos, S.; Lafosse, X.; Coolen, L.; Schwob, C.; Javaux, C.; *et al.* Controlling Spontaneous Emission with Plasmonic Optical Patch Antennas. *Nano Lett.* **2013**, *13*, 1516–1521.
10. Vecchi, G.; Giannini, V.; Gómez Rivas, J. Shaping the Fluorescent Emission by Lattice Resonances in Plasmonic Crystals of Nanoantennas. *Phys. Rev. Lett.* **2009**, *702*, 2–5.
11. Lozano, G.; Louwers, D. J.; Rodriguez, S.; Murai, S.; Jansen, O. T. A.; Verschuuren, M.; Rivas, J. G. Plasmonics for Solid-State Lighting: Enhanced Excitation and Directional Emission of Highly Efficient Light Sources. *Light: Sci. Appl.* **2013**, *2*, e66.
12. Busch, K.; John, S. Photonic Bandgap Formation in Certain Selforganizing Systems. *Phys. Rev. E* **1998**, *58*, 3896–3908.
13. Koenderink, A. R; Bechger, L.; Schriemer, H. P.; Lagendijk, A.; Vos, W. L. Broadband Five fold Reduction of Vacuum Fluctuations Probed by Dyes in Photonic Crystals. *Phys. Rev. Lett.* **2002**, *88*, 143903.
14. Fujita, M.; Takahashi, S.; Tanaka, Y.; Takashi, A.; Noda, S. Simultaneous Inhibition and Redistribution of Spontaneous Light Emission in Photonic Crystals. *Science* **2005**, *308*, 1296–1298.
15. Lodahl, P.; van Driel, A. R.; Nikolaev, I. S.; Irman, A.; Overgaag, K.; Vanmaekelbergh, D.; Vos, W. L. Controlling the Dynamics of Spontaneous Emission from Quantum Dots by Photonic Crystals. *Nature* **2004**, *430*, 654–657.
16. Wang, Q.; Stobbe, S.; Lodahl, P. Mapping the Local Density of Optical States of a Photonic Crystal with Single Quantum Dots. *Phys. Rev. Lett.* **2011**, *707*, 167404.
17. Jorgensen, M. R.; Galusha, J. W.; Bartl, M. H. Strongly Modified Spontaneous Emission Rates in Diamond-Structured Photonic Crystals. *Phys. Rev. Lett.* **2011**, *707*, 143902.
18. Noda, S.; Fujita, M.; Asano, T. Spontaneous-Emission Control by Photonic Crystals and Nanocavities. *Nat. Photonics* **2007**, *7*, 449–458.
19. Barth, M.; Niisse, N.; Löchel, B.; Benson, O. Controlled Coupling of a Single-Diamond Nanocrystal to a Photonic Crystal Cavity. *Opt. Lett.* **2009**, *34*, 1108–1110.
20. Aoki, K.; Guimard, D.; Nishioka, M.; Nomura, M.; Iwamoto, S.; Arakawa, Y. Coupling of Quantum-Dot Light Emission with a Three-Dimensional Photonic-Crystal Nanocavity. *Nat. Photonics* **2008**, *2*, 688–692.
21. Noda, S. Photonic Crystal Lasers - Ultimate Nanolasers and Broad-Area Coherent Lasers [Invited]. *J. Opt. Soc. Am. B* **2010**, *27*, B1–B8.
22. Mertens, H.; Koenderink, A. E; Polman, A. Plasmon-Enhanced Luminescence Near Noble-Metal Nanospheres: Comparison of Exact Theory and an Improved Gersten and Nitzan Model. *Phys. Rev. B* **2007**, *76*, 115123.
23. Ming, T.; Zhao, L.; Chen, H.; Woo, K. C; Wang, J.; Lin, H.-Q. Experimental Evidence of Plasmophores: Plasmon-Directed Polarized Emission from Gold Nanorod-Fluorophore Hybrid Nanostructures. *Nano Lett.* **2011**, *77*, 2296–2303.
24. Ming, T.; Chen, H.; Jiang, R.; Li, Q.; Wang, J. Plasmon-Controlled Fluorescence: Beyond the Intensity Enhancement. *J. Phys. Chem. Lett.* **2012**, *3*, 191–202.
25. Wedge, S.; Hooper, I. R.; Sage, I.; Barnes, W. L. Light Emission through a Corrugated Metal Film: The Role of Cross-Coupled Surface Plasmon Polaritons. *Phys. Rev. B* **2004**, *69*, 245418.
26. Rodriguez, S.; Murai, S.; Verschuuren, M.; Gómez Rivas, J. Light-Emitting Waveguide-Plasmon Polaritons. *Phys. Rev. Lett.* **2012**, *709* (166803), 1–5.
27. Zayats, A. V.; Smolnyaninov, I. L; Maradudin, A. A. Nano-Optics of Surface Plasmon Polaritons. *Phys. Rep.* **2005**, *408*, 131–314.
28. Ebbesen, T. W.; Lezec, H. J.; Ghaemi, H. R; Thio, T.; Wolff, P. A. Extraordinary Optical Transmission through Sub-Wavelength Hole Arrays. *Nature* **1998**, *391*, 667–669.
29. Garcia de Abajo, F. J. Colloquium: Light Scattering by Particle and Hole Arrays. *Rev. Mod. Phys.* **2007**, *79*, 1267–1290.
30. Garcia-Vidal, F. J.; Ebbesen, T. W.; Kuipers, L. Light Passing through Subwavelength Apertures. *Rev. Mod. Phys.* **2010**, *82*, 729–787.
31. Przybilla, R.; Degiron, A.; Genet, C.; Ebbesen, T.; de Léon-Pérez, R.; Bravo-Abad, J.; García-Vidal, F. J.; Martín-Moreno, L. Efficiency and Finite Size Effects in Enhanced Transmission through Subwavelength Apertures. *Opt. Express* **2008**, *16*, 9571–9579.

32. Henzie, J.; Lee, M. H.; Odom, T. W. Multiscale Patterning of Plasmonic Metamaterials. *Nat. Nanotechnol.* **2007**, *2*, 549–554.
33. Kitson, S.; Barnes, W.; Sambles, J. Full Photonic Band Gap for Surface Modes in the Visible. *Phys. Rev. Lett.* **1996**, *77*, 2670–2673.
34. Barnes, W. L.; Kitson, S. C; Preist, T. W.; Sambles, J. R. Photonic Surfaces for Surface-Plasmon Polaritons. *J. Opt. Soc. Am. A* **1997**, *14*, 1654.
35. Lalanne, P.; Rodier, J. C.; Hugonin, J.-P. Surface Plasmons of Metallic Surfaces Perforated by Nanoholes. *J. Opt. A - Pure Appl. Opt.* **2005**, *7*, 422–426.
36. Jun, Y. C; Huang, K. C. Y.; Brongersma, M. L. Plasmonic Beaming and Active Control Over Fluorescent Emission. *Nat. Commun.* **2011**, *2*, 283.
37. Verschuuren, M.; Gerlach, P.; van Sprang, H. A.; Polman, A. Improved Performance of Polarization-Stable VCSELs by Monolithic Sub-Wavelength Gratings Produced by Soft Nano-Imprint Lithography. *Nanotechnology* **2011**, *22*, 505201.
38. Nagpal, P.; Lindquist, N. C.; Oh, S. H.; Norris, D. J. Ultrasmooth Patterned Metals for Plasmonics and Metamaterials. *Science* **2009**, *325*, 594–597.
39. Henzie, J.; Lee, J.; Lee, M. H.; Hasan, W.; Odom, T. W. Nanofabrication of Plasmonic Structures. *Annu. Rev. Chem.* **2009**, *60*, 147–165.
40. Schwille, P.; Bieschke, J.; Oehlenschlager, F. Kinetic Investigations by Fluorescence Correlation Spectroscopy: The Analytical and Diagnostic Potential of Diffusion Studies. *Biophys. Chem.* **1997**, *66*, 211–228.
41. Novotny, L.; Hecht, B. *Principles of Nano Optics*; Cambridge University Press, 2006.
42. Sersic, I.; Tuambilangana, C.; Koenderink, A. F. Fourier Microscopy of Single Plasmonic Scatterers. *New J. Phys.* **2011**, *13*, 083019.
43. Balanis, C. A. *Antenna Theory: Analysis and Design*, 3rd ed.; John Wiley & Sons: Hoboken, NJ, 2005.
44. Rigneault, H.; Lemarchand, F.; Sentenac, A.; Giovannini, H. Extraction of Light from Sources Located inside Waveguide Grating Structures. *Opt. Lett.* **1999**, *24*, 148–150.
45. Harrison, W. A. *Solid State Theory*; Dover Publications, 1970.
46. Kretschmann, M.; Maradudin, A. Band Structures of Two-Dimensional Surface-Plasmon Polaritonic Crystals. *Phys. Rev. B* **2002**, *66*, 245408.
47. Nikolaev, I.; Lodahl, P.; Vos, W. Quantitative Analysis of Directional Spontaneous Emission Spectra from Light Sources in Photonic Crystals. *Phys. Rev. A* **2005**, *71*, 053813.
48. Barth, M.; Gruber, A.; Cichos, F. Spectral and Angular Redistribution of Photoluminescence Near a Photonic Stop Band. *Phys. Rev. B* **2005**, *72*, 085129.
49. Garcia-Santamaria, R.; Galisteo-López, J. R; Braun, P. V.; López, C. Optical Diffraction and High-Energy Features in Three-Dimensional Photonic Crystals. *Phys. Rev. B* **2005**, *71*, 195112.
50. Galisteo-López, J. R.; Galli, M.; Patrini, M.; Balestreri, A.; Andreani, L. C.; López, C. Effective Refractive Index and Group Velocity Determination of 3D Photonic Crystals by Means of White Light Interferometry. *Phys. Rev. B* **2006**, *73*, 125103.
51. Li, Z.-Y.; Zhang, Z.-Q. Weak Photonic Band Gap Effect on the Fluorescence Lifetime in Three-Dimensional Colloidal Photonic Crystals. *Phys. Rev. B* **2001**, *63*, 125106.
52. Nikolaev, I.; Lodahl, P.; Vos, W. Fluorescence Lifetime of Emitters with Broad Homogeneous Linewidths Modified in Opal Photonic Crystals. *J. Phys. Chem. C* **2008**, *772*, 7250–7254.
53. Wenger, J.; Gérard, D.; Dintinger, O., J.; Mahboub; Bonod, N.; Popov, E.; Ebbesen, T. W.; Rigneault, H. Emission and Excitation Contributions to Enhanced Single Molecule Fluorescence by Gold Nanometric Apertures. *Opt. Express* **2008**, *16*, 3008.
54. Saleh, B. E. A.; Teich, M. C. *Fundamentals of Photonics*, 2nd ed.; Wiley and Sons: Hoboken, NJ, 2007; Chapter 4.
55. Penninkhof, J. J.; Moroz, A.; van Blaaderen, A.; Polman, A. Optical Properties of Spherical and Oblate Spheroidal Gold Shell Colloids. *J. Phys. Chem. C* **2008**, *772*, 4146–4150.
56. Taflove, A.; Hagness, S. C. *Computational Electrodynamics: The Finite-Difference Time-Domain Method*, 3rd ed.; Artech House Publishers, 2005; Chapter 8.
57. Lukosz, W.; Kunz, R. E. Light Emission by Magnetic and Electric Dipoles Close to a Plane Interface. I. Total Radiated Power. *J. Opt. Soc. Am.* **1977**, *67*, 1607–1615.
58. Lukosz, W.; Kunz, R. E. Light Emission by Magnetic and Electric Dipoles Close to a Plane Dielectric Interface. II. Radiation Patterns of Perpendicular Oriented Dipoles. *J. Opt. Soc. Am.* **1977**, *67*, 1615–1619.